Geophysical Journal International

*Geophys. J. Int.* (2026) **246,** 1–17
Advance Access publication 2026 July 16
Research paper

https://doi.org/10.1093/gji/ggag285

# Direction monitoring of secondary microseismic noise for Love and Rayleigh waves with a single six-degree-of-freedom station

Andreas Brotzer [1], Heiner Igel,[1] Felix Bernauer,[1] Joachim Wassermann,[1] Céline Hadziioannou [2] and Karl Ulrich Schreiber[3]

[1]*Department of Earth and Environmental Sciences, Ludwig-Maximilians-Universität München, Theresienstrasse 41, 80333 Munich, Germany. E-mail.andbro@tutanota.com.*
[2]*Department of Earth System Science - Geophysics, University of Hamburg, Bundesstrasse 55, 20146 Hamburg, Germany*
[3]*Research Unit Satellite Geodesy, Technical University of Munich, Sackenrieder Straße 25, 93444 Bad Kötzting, Germany*

Accepted 2026 July 13. Received 2026 July 3; in original form 2026 April 10

## SUMMARY

Knowing and monitoring the spatial distribution of ambient seismic noise sources is essential for correlation-based investigations in seismology. The omnipresent primary and secondary microseismic noise characterizes the ocean-generated noise of the seismic spectrum and has been studied through observations and modelling to better constrain the source mechanisms, the source regions, and their temporal variability. In this study, we demonstrate the potential of a single six-degree-of-freedom (6-DoF) station, observing co-located translational and rotational ground motions, to determine and continuously monitor the source directions of the secondary microseismic wavefield. We harness direct rotational ground motion data obtained with the ROtational Motions in seismologY ring laser array. The effective array-like capability of a single 6-DoF station to separate Love and Rayleigh waves, both constituents of the secondary microseismic wavefield, by their polarization enables the independent estimation of the dominant source directions and the monitoring of their seasonal evolution. An anticipated seasonality is evident, with a dominant source direction for Love (254°) and Rayleigh (277°) waves in winter, whereas in summer no clear dominant direction emerges due to an absence of strong nearby sources. We compare 6-DoF-based backazimuth estimates with those of seismic array beamforming and find close agreement concerning the dominant source directions, particularly in the case of migrating pelagic storms in the North Atlantic associated with strong ocean wave activity over several days. In winter, a systematic bias of about 25° to 35° for Rayleigh waves and 50° for Love waves is identified between the 6-DoF-based backazimuth estimates and those inferred for significant wave heights obtained from satellite altimetry and model-based seismic noise source maps. Our results provide a proof-of-concept for the direction monitoring of the secondary microseismic noise for both Love and Rayleigh waves using direct rotational observations, thereby reducing reliance on array-based estimates. The advent of portable high-sensitive rotation sensors will facilitate constraining spatial seismic noise source distributions and temporal variations therein with future 6-DoF station networks potentially replacing or complementing traditional seismic array deployments.

**Key words:** Rotational seismology; Seismic noise; Seismic instruments; Polarization analysis; Time-series analysis; Site effects.

## 1 INTRODUCTION

Monitoring the distributions of ambient seismic noise sources is essential for noise-based methodologies in seismology. Microseisms are an omnipresent source in the seismic noise spectrum of the Earth, documenting the persistent interaction between the Earth's oceans and the solid Earth. Since early instrumental seismic observations, the coherent and omnipresent seismic noise has been discussed and traced to ocean waves and coastal surf (E. Wiechert 1904; B. Gutenberg 1912, 1921, 1936). A first explanation for the generation of secondary microseisms was introduced by M.S. Longuet-Higgins (1950) and expanded for primary microseisms based on a statistical approach by K. Hasselmann (1963). Primary microseismic noise (0.05–0.1 Hz) is generated by the interaction of ocean swell with coastlines, with coastal shelf regions or with bathymetric features (e.g. K. Hasselmann 1963; F. Ardhuin *et al.* 2015; L. Gualtieri *et al.* 2019; T. Tanimoto & A. Anderson 2023). The secondary microseismic noise, in a band of 0.1–0.3 Hz, however, is generated by the nonlinear wave–wave interaction of oceanic gravity surface waves, which causes pressure perturbations at the seafloor, exciting seismic waves (e.g. M.S. Longuet-Higgins 1950; F. Ardhuin *et al.* 2015; T. Tanimoto & A. Anderson 2023). When oceanic surface waves or swell, generally caused by pelagic storms, interfere in parts of the storm system where the waves are comparable in size and frequency as well as approximately counter-propagating, a pressure variation at the seafloor is excited that radiates seismic waves. The

© The Author(s) 2026. Published by Oxford University Press on behalf of The Royal Astronomical Society. This is an Open Access article distributed under the terms of the Creative Commons Attribution License (https://creativecommons.org/licenses/by/4.0/), which permits unrestricted reuse, distribution, and reproduction in any medium, provided the original work is properly cited.



Downloaded from academic.oup.com/gji/article/246/3/ggag285/8736044 by guest on 03 October 2026

clash of high-amplitude waves, resulting in a frequency shift for the seismic waves with regard to the generating ocean waves, can be explained with nonlinear interaction. The location and magnitude of generated secondary microseismic noise may vary over the lifetime of a pelagic storm of several days as the occurrence of opposing, similar gravity waves varies.

To study the source regions and mechanisms of the primary and the secondary microseism observations with a single seismic station or a seismic array, as well as varying methodologies have been employed (e.g. R.K. Cessaro 1994; A. Friedrich *et al.* 1998; H.H. Essen *et al.* 2003; S. Chevrot *et al.* 2007; M. Schimmel *et al.* 2011; C. Hadziioannou *et al.* 2012; G. Hillers *et al.* 2012; C. Juretzek & C. Hadziioannou 2016, 2017; M. Safarkhani *et al.* 2025). Numerical modelling provided a better understanding of the energy partitioning and source distribution (e.g. E. Stutzmann *et al.* 2012; L. Gualtieri *et al.* 2015; J.K.H. Igel *et al.* 2021b). The secondary microseism wavefield excites both Love and Rayleigh waves, while their energy partitioning, expressed as the Love-to-Rayleigh (L/R), ratio varies regionally, commonly between 0.5 and 1.2 (e.g. T. Tanimoto *et al.* 2015, 2016; F. Le Pape *et al.* 2021).

The energy partitioning of Love and Rayleigh waves in the secondary microseism band has been studied and modelled, but is still not entirely understood (e.g. T. Tanimoto *et al.* 2015; C. Juretzek & C. Hadziioannou 2016; L. Gualtieri *et al.* 2021; F. Le Pape et al. 2021). L. Gualtieri *et al.* (2015) conclude that the ocean depth and sedimentary structure at the pelagic source region shape the mode content of Rayleigh waves, where shallower regions promote fundamental modes, while deeper water enhances the first overtone. Thick sedimentary layers at the source region decrease the amplitude of emitted seismic waves (L. Gualtieri *et al.* 2021). From numerical studies, it is concluded that wave type conversions along the propagation path would not be sufficient to explain the Love-to-Rayleigh ratios observed in the secondary microseism (D. Ziane & C. Hadziioannou 2019).

In the context of rotational seismology or seismic gradiometry, the observation of six degrees-of-freedom (6-DoF) motions of the seismic wavefield is achieved through the combination of a co-located broad-band translation (e.g. seismometer) and rotation (rate) sensor (e.g. ring laser gyroscope) or alternatively using array-derived rotations (A. Cochard *et al.* 2006; C.A. Langston & C. Liang 2008; P. Spudich & J.B. Fletcher 2008; H. Igel *et al.* 2014). This provides an information gain on the seismic wavefield at a single station, comparable to that of a seismic array, such as the local phase velocity structure or the propagation direction (e.g. A. Pancha *et al.* 2000; A. Cochard *et al.* 2006; H. Igel *et al.* 2014; C. Schmelzbach *et al.* 2018; D. Sollberger *et al.* 2020; S. Keil *et al.* 2021; K. Kislov & V. Gravirov 2021).

Using data of a one-component large-scale ring laser gyroscope (G-ring), C. Hadziioannou *et al.* (2012) examined the recorded secondary microseismic noise, however, being limited to rotations around a vertical axis, thus only sensitive to *SH*-type and Love waves. ROMY (ROtational Motions in seismologY) is an unprecedented geophysical instrument and at this point, the only sensor that provides direct observations of weak rotational ground motion for *all three rotational components*, hence a *full* 6-DoF station (H. Igel *et al.* 2021a). In contrast to the single-component G-ring laser gyroscope (K.U. Schreiber *et al.* 2009), ROMY is composed of four independent, triangular-shaped, large-scale ring laser gyroscopes that are assembled into a tetrahedron (H. Igel *et al.* 2021a). ROMY is located at the Geophysical Observatory in Fürstenfeldbruck (Germany), therefore sits in the pre-alpine sedimentary Molasse basin (e.g. G.H. Bachmann & M. Müller 1992).

The potential of seismic source tracking with single-station 6-DoF methods, in particular for earthquake rupture tracking, was outlined by H. Igel *et al.* (2014); S. Yuan *et al.* (2021, 2025) with a focus on synthetic and some observation data, as high-sensitive rotation sensors are still scarce (e.g. F. Bernauer *et al.* 2012a; A. Brotzer *et al.* 2024), and mostly limited to *SH*-type or Love waves. 6-DoF backazimuth estimation methods were successfully applied for nearby traffic (e.g. S. Yuan *et al.* 2021), artificial sources (e.g. G. Izgi *et al.* 2025), local and regional seismicity (e.g. S. Yuan *et al.* 2020; J. Wassermann *et al.* 2022; A. Brotzer *et al.* 2025b), teleseismic earthquakes (e.g. A. Pancha *et al.* 2000; H. Igel *et al.* 2005) and ambient seismic noise (C. Hadziioannou *et al.* 2012). L. Tang *et al.* (2024) recently used array-derived rotations (ADR) based on a seismic array in Southern California to constrain the seasonality of secondary microseisms with a single *ADR-based* 6-DoF station.

With direct 6-DoF observations, we extend the study of C. Hadziioannou *et al.* (2012) to *SV*-type and Rayleigh waves, in addition to Love or *SH*-type waves, for a 1.5-yr-long observation interval. The secondary microseismic peak is present for ROMY throughout the year (Fig. S5, Supplementary Material), whereas the primary microseismic peak still remains below the sensor's current self-noise level and only appears during periods of strong excitation.

In this proof-of-concept study, we demonstrate the potential of the 6-DoF polarization-based methodology to identify and monitor the direction of secondary microseism source regions for Love and Rayleigh waves separately. This is the first time this can be demonstrated for a single 6-DoF station with *direct* rotational measurements of all three components. In terms of the knowledge of locating omnipresent seismic noise sources, future seismic networks equipped with 6-DoF stations ('arrays-of-arrays') are valuable, once three-component, *portable*, high-sensitive rotation sensors become available.

Beyond the introduction, this study is structured as follows: In Section 2, we present the data set and describe basic data processing. Section 3 describes the 6-DoF methodology employed to obtain backazimuth from seismic and reference data. In Section 4, we identify the dominant backazimuth direction for Rayleigh and Love polarization in winter and summer, which is validated using directivity determination with classical seismic array processing methods and source locations inferred from satellite images of wave heights, as well as inversion-based source maps. Directional monitoring of a pelagic storm system is demonstrated and discussed therein. Finally, the results are discussed (Section 5) and concluded (Section 6).

Downloaded from academic.oup.com/gji/article/246/3/ggag285/8736044 by guest on 03 October 2026

## 2 DATA AND PROCESSING

The multisensor data set used in this study, ranging from 2024 January 01 to 2025 June 30, is explained in this section. It comprises seismic rotational motion data, seismic translation data and significant wave height satellite data. Basic data processing that is applied is described or referenced.

### 2.1 Rotational ground motion data

ROMY was built to demonstrate the potential of 6-DoF seismological observations with weak rotational ground motions (H. Igel *et al.* 2021a). The processing chain to obtain rotation rate measurements of ROMY's optical Sagnac interferometer gyroscopes is explained in detail in H. Igel *et al.* (2021a).

Technical upgrades are required for the prototype sensor, using optical Sagnac interferometry to sense rotation rates, to fully mitigate design-related mechanical instabilities and environmental influences that currently affect continuous seismic recordings at the highest quality (A. Brotzer *et al.* 2025a). Consequently, the data set exhibits data gaps in one or multiple components, yet it remains the longest data set obtained at high quality so far. In order to obtain the horizontal components of rotation (north and east), three ring laser gyroscopes have to be operated simultaneously. With an independent ring laser gyroscope for the vertical component of rotation, fewer data gaps are present for this component. The operation and quality assessment logs of ROMY provide information on known instrumental glitches and outages, which are used to reject data. A longer data gap between 2024-December-24 and 2025-April-11 results from an extensive maintenance activity.

Throughout the year of 2024, an increase in continuous record (above 80 per cent uptime) with high data quality was achieved for three of ROMY's gyroscopes ($U$, $V$ and $Z$ components; A. Brotzer *et al.* (2025a)). This makes a 6-DoF seismic noise study using ROMY data between 2024 January 1 and 2025 June 30, possible.

### 2.2 Translational ground motion data

The three-component translational data for the 6-DoF station is provided by the German regional seismic network station GR.FUR in Fürstenfeldbruck, which is a broad-band three-component Streckeisen STS-2.5 seismometer located in an underground vault about 10 m west of ROMY. Station data in parts of August and September 2024 are not available due to maintenance activity. A small-aperture seismic array (4.2 km aperture), consisting of six broad-band STS-2 seismometer surface stations (GR.FUR, BW.GELB. BW.ALFT, BW.GRMB, BW.TON, BW.BIB; G.H. BayernNetz 2001), surrounds ROMY and is used to determine backazimuths based on the established array-based f–k beamforming (P. Bormann 2012) to serve as an independent validation. For the observation period of this study, data from the station BW.ALFT were not available, effectively reducing the array to five stations.

### 2.3 Significant wave height data

Satellite images using altimetry to measure the significant wave heights (SWHs) are a common proxy to locate maximal ocean wave activity, which is linked to the pelagic source regions generating secondary microseismic noise (e.g. H.H. Essen *et al.* 2003; H.S. Shabtian *et al.* 2023). For our study, processed SWH images are obtained from the E.U. Copernicus Marine Service (CMEMS) via the Marine Data Store as global ocean level 4 (L4) SWH images from Nrt satellite measurements (https://doi.org/10.48670/moi-00180). The daily maximum SWH images, with a spatial resolution of 2° by 2°, are used to provide a reference for the location of maximal ocean wave activity. A 2-D, spatial low-pass filter (3×3 pixels) is applied to smooth the images and fill blank spaces.

## 3 METHODOLOGY

As a result of the linear, elastic theory for homogeneous isotropic media, the seismic wavefield consists not only of translational ground motions, but also of the wavefield gradients: three components of rotational motions and up to six independent components for strain. The seismic wavefield gradients are required to fully describe the seismic wavefield and provide additional insight into the local subsurface (e.g. M. Bernauer *et al.* 2012b; H. Igel *et al.* 2014; S. Singh 2020). The rotational motion ($\boldsymbol{\omega} = (\omega_x, \omega_y, \omega_z)^T$) is defined as the curl of the displacement wavefield $\boldsymbol{u} = (u_x, u_y, u_z)^T$:

$$\begin{pmatrix} \omega_x \\ \omega_y \\ \omega_z \end{pmatrix} = \frac{1}{2} \nabla \times \mathbf{u} = \frac{1}{2} \begin{pmatrix} \partial_y u_z - \partial_z u_y \\ \partial_z u_x - \partial_x u_z \\ \partial_x u_y - \partial_y u_x \end{pmatrix}, \tag{1}$$

with $\times$ indicating a vector product and $\partial_i$ denoting the spatial derivative in direction $i \in [x, y, z]$ (e.g. A. Pancha *et al.* 2000; A. Cochard *et al.* 2006). By observing the three components of translations (with a seismometer) and the three components of rotations (with a rotation sensor or gyroscope) co-located, a 6-DoF station can be defined, and a more complete observation of the seismic wavefield is obtained.

Downloaded from academic.oup.com/gji/article/246/3/ggag285/8736044 by guest on 03 October 2026

### 3.1 6-DoF backazimuth estimation

When assuming plane wave propagation, the backazimuth provides an estimate of the source direction along a great circle path. To study the temporal variation of the backazimuth, continuous waveform data are analysed and bandpass filtered between 0.1 and 0.15 Hz (10 and 6.7 s period) to capture the secondary microseismic peak. Modules of the ObsPy package are used for most waveform processing (M. Beyreuther *et al.* 2010). The backazimuth estimation is performed in short time windows of 49 s, corresponding to six times the central period ($1/f_c = 1/\sqrt{f_{\min} \cdot f_{\max}}$), with an overlap of 75 per cent. Backazimuth estimates are obtained for 6-DoF data using the three different approaches, as explained in the following sections, while f–k array beamforming (for translation array data) is used as an independent method for validation purposes.

#### *3.1.1 Grid search correlation approach*

With a single 6-DoF station, the component combination of the vertical translation acceleration ($a_Z$) and the transverse rotational velocity ($\dot{\omega}_T$) or the vertical rotational velocity ($\dot{\omega}_Z$) and the transverse translational acceleration ($a_T$) allows distinguishing between the Rayleigh and Love contributions of the seismic wavefield, respectively. Because rotational velocity and translational acceleration are in phase according to a plane wave in elastic theory (e.g. A. Cochard *et al.* 2006), a grid search in backazimuth increments (here 1°) can be used to optimize the cross-correlation of the waveforms and determine the optimal backazimuth. Hence, it is based on a phase match and hereafter referred to as *Rayleigh* and *Love* method, depending on the used components.

The normalized, zero-lag cross-correlation (CC) value, ranging from −1 (anticorrelation) to 1 (correlation), hereby serves as a quantitative measure of waveform similarity. Instead of determining the maximum of the CC values (e.g. H. Igel *et al.* 2007), the backazimuth is estimated by determining the midpoint between the zero-crossings of the computed CC function (e.g. S. Yuan *et al.* 2021). Dividing the waveforms into time windows enables temporal tracking of the incident plane-wave directions.

#### *3.1.2 Tangent approach*

For a travelling plane wave, the backazimuth ($\Phi_{\text{baz}}$) can be estimated using *SV*-type and Rayleigh waves using the horizontal components of a single station with a polarization approach (E. Flinn 1965):

$$\Phi_{\text{baz}} = -\arctan\left(\frac{\dot{\omega}_{\text{N}}}{\dot{\omega}_{\text{E}}}\right), \tag{2}$$

with $\dot{\omega}_{\text{N}}$ and $\dot{\omega}_{\text{E}}$ referring to the north–south and east–west rotational components, respectively. To obtain a positive estimate, 180° is added to shift the negative backazimuth into a range of 0°–180°. With a single station using translational motions, a 180° ambiguity remains. Using $\Phi_{\text{baz}}$ (and $\Phi_{\text{baz}} \pm 180°$) to obtain two transverse rotational velocities ($\dot{\omega}_T$) and correlated it with the vertical translational acceleration ($a_Z$), reveals the true backazimuth with a positive correlation. If the correlation is positive, 180° are added to $\Phi_{\text{baz}}$. This is not feasible with a translational station only. In the employed algorithm, the covariance matrix is determined for each time window estimate. The ratio of the first eigenvalue for the rotational north and east components used for the backazimuth estimation to increase the robustness of the estimate (e.g. S. Yuan *et al.* 2021; J. Wassermann *et al.* 2022; S. Yuan *et al.* 2025). This eigenvalue-based polarization analysis, originally introduced by E. Flinn (1965), is referred to as the *Tangent method* in this study. Exploiting the horizontal rotational components, it provides an alternative to the Rayleigh-based grid search approach using the same wavefield information.

#### *3.1.3 Array beamforming*

Seismic array beamforming is an established method to determine the direction of seismic waves using array data (P. Bormann 2012). The ObsPy implementation of a one-component beamforming analysis in the frequency–wavenumber (f–k) domain (M. Beyreuther *et al.* 2010) is used to obtain backazimuth estimates for the seismic array surrounding ROMY to validate the results of the 6-DoF methods. As expected, the horizontal components of the surface stations exhibit significantly higher noise levels than the vertical components. Therefore, we focus on the vertical component for backazimuth estimates, thus associated with Rayleigh waves, which we use as a validation reference.

#### *3.1.4 Estimated hourly backazimuths*

Based on the assumption that the location of secondary microseisms does not change significantly within one hour, a statistical estimation for hourly time intervals is computed. In case that more than five backazimuths with a CC value above a set threshold of 0.8 exist within one hour, the peak-based backazimuth and the covariance of a probability density function (PDF) are determined, using a Gaussian kernel density estimation (KDE). The CC values are assigned as weights for the PDF and the covariance computation (see Fig. 1). Possible estimation errors on the backazimuth for values close to 0° or 360° are compensated. This results in a robust weighted backazimuth estimate for one hour with an uncertainty.

Downloaded from academic.oup.com/gji/article/246/3/ggag285/8736044 by guest on 03 October 2026

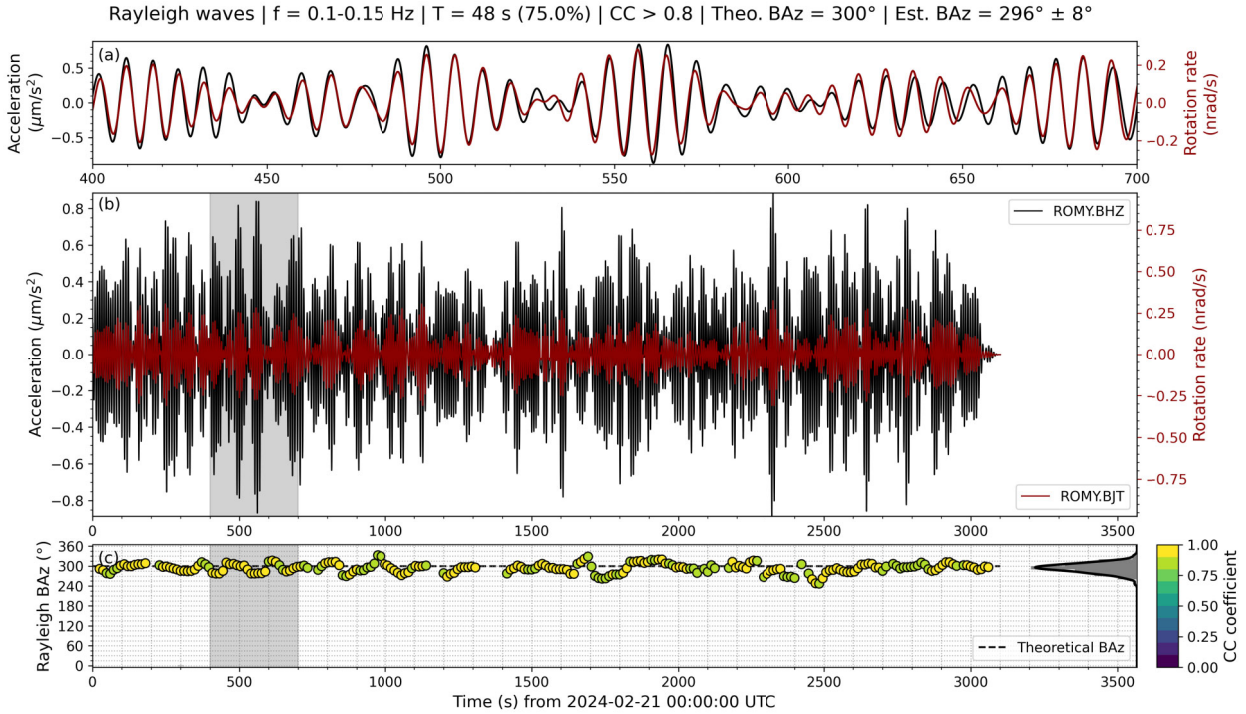


**Figure 1.** (a) A selected time period (shaded area) of (b) waveforms for an entire hour, showing the vertical translational acceleration of FUR (black) and transverse rotation rate of ROMY (red), hence Rayleigh waves, on 2024-February-21. The data are filtered between 0.1 and 0.15 Hz. The lower panel shows the backazimuth estimates in 42 s time windows (with 75 per cent overlap) based on the Rayleigh wave grid search approach and colour-coded by the CC coefficient of each time window. Only estimates above a CC threshold of 0.8 are displayed. At the right end of the panel, the weighted histogram (shaded) and probability density function (solid line), used to estimate a backazimuth of 299°± 10°, are shown. The theoretical backazimuth (dashed line) is set to300° to obtain a transverse waveform, as shown in panels (a) and (b).

For the tangent method, no weights are applied for computing the histogram and determining the statistical hourly backazimuth estimate. As no CC value is computed for the beamforming method, the obtained relative power is used as weights for the histogram computation.

### 3.2 Expected backazimuths for validation

We compare our seismological results with source directions inferred from maps of average maximal SWHs from satellite altimetry measurements, acknowledging that SWHs are not exactly equivalent to maps of seismic wave generation (G. Hillers *et al.* 2012), however, they can act as a proxy for regions where high seismic noise generation is expected. The obtained and smoothed global SWH satellite data are employed to estimate the peak activity and the corresponding backazimuth relative to the 6-DoF station. A first approach determines the peak activity on the global SWH map and the corresponding backazimuth. This straightforward approach does not discriminate between equally strong regions of activity based on their distance to the station. As an alternative estimate, the SWH pixels are integrated in 10° backazimuth bins and weighted by the normalized wave height and inverse source–receiver distance ($R^{-1}$). The maximum of the dominant mode of the corresponding KDE is identified as the backazimuth, and its associated uncertainty is quantified as half the median absolute deviation around this peak.

A comparison of these two approaches is provided for three representative examples in the Supplementary Materials (Figs S7a–c). On some days, backazimuth estimates derived from the simple peak-activity identification are consistent with those from the distance-weighted integration (Supplementary Figs S7a and c), whereas on other days they exhibit substantial discrepancies (Supplementary Fig. S7b). Estimating a dominant backazimuth from globally distributed sources with distance weights proportional to $R^{-1}$ reveals several preferred directions for the integrated wave activity (Supplementary Fig. S9b). More similar results are obtained for both approaches in winter, while for a majority of days, the results disagree. Especially in summer, the peak-activity identification points to the oceans of the Southern Hemisphere with backazimuths of 110°–240°. Overall, the weighted integration approach yields more stable backazimuth estimates, with typical uncertainties between ±30° and ±40°. Furthermore, the method can be tuned to emphasize regional activity by modifying the distance weighting scheme. Enhancing the contribution of nearby sources ($R^{-2}$) shifts the dominant backazimuths to the range 270°–10° (Fig. S9a, Supplementary Material).

As an additional reference, we utilize the global seismic noise source maps generated daily with a seismic finite-frequency inversion scheme using globally distributed broad-band stations (J.K.H. Igel *et al.* 2021b). Specifically, we employ the publicly available daily

Downloaded from academic.oup.com/gji/article/246/3/ggag285/8736044 by guest on 03 October 2026

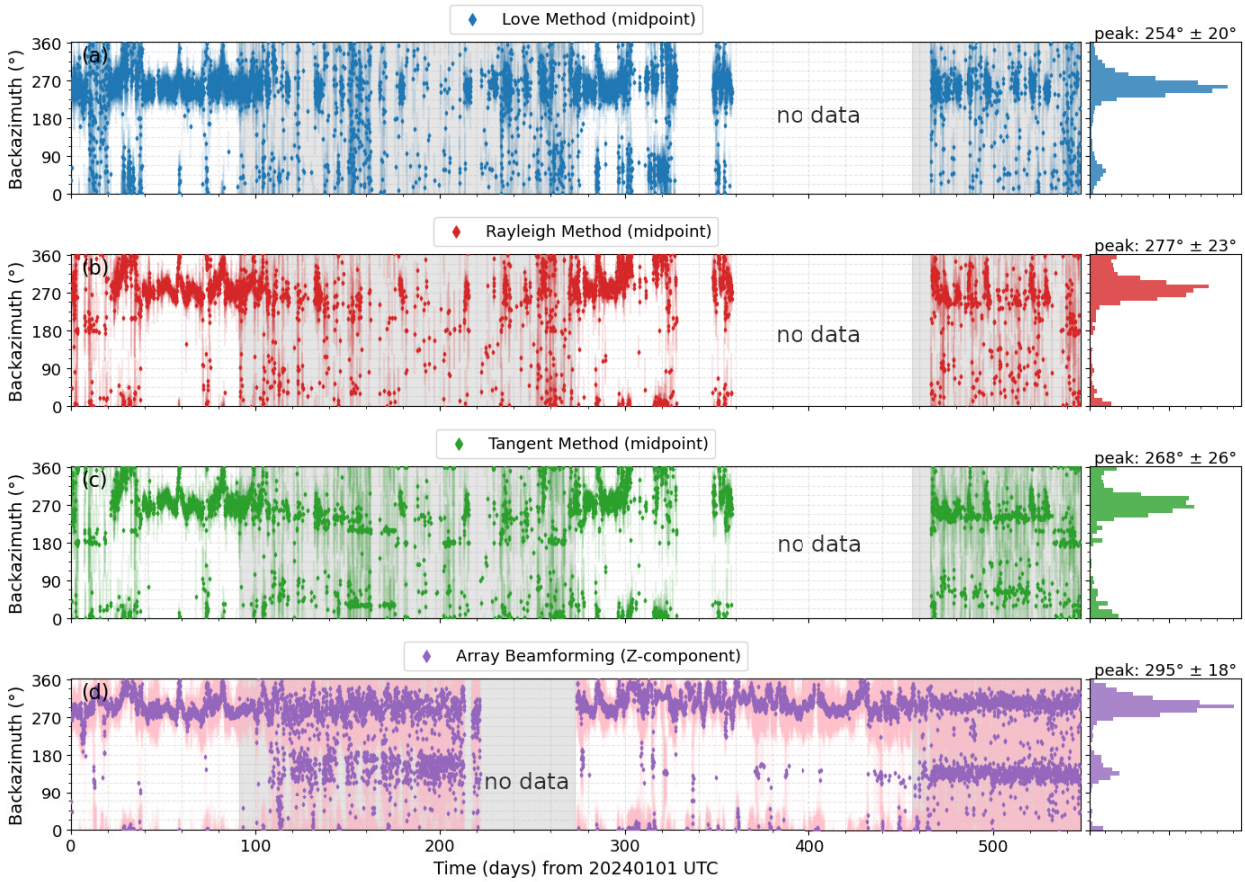


**Figure 2.** Hourly backazimuth estimates with standard deviations are shown between 2024-January-01 and 2025-June-30 using (a) the Love method, (b) the Rayleigh method, (c) the Tangent method (Rayleigh waves), and (d) array beamforming with the vertical component (Rayleigh waves), with shaded error envelopes. The grey-shaded background indicates the summer months (April to September) of the Northern Hemisphere.

multiscale seismic ambient noise source (SANS) maps (J.K.H. Igel *et al.* 2023), which cover about 50 per cent of the observation interval (265 d in 2024 and 9 d in 2025). These maps serve as an additional constraint on the expected dominant backazimuth directions, which are inferred using the same approaches as for the SWH data (Fig. S9c, Supplementary Material). Three exemplary estimates for both methods are shown in Fig. S8 in the Supplementary Material with pronounced activity peaks.

## 4 RESULTS

### 4.1 Seasonal variations

Seasonal variations of the dominant source locations for secondary microseisms are expected between summer and winter due to a variation in the global pelagic storm activity and therefore ocean wave height distribution (e.g. F. Ardhuin *et al.* 2011; E. Stutzmann *et al.* 2012; L. Gualtieri *et al.* 2019). For this study, the summer months on the Northern Hemisphere are defined as the period from April 01 to September 30.

Hourly estimates and their estimated standard deviations are shown for all four methods over an observation period from 2024 January 01 to 2025 June 30 (limited by observations of ROMY) in Fig. 2. The summer months are indicated by a grey-shaded background.

For all four methods, the summer months show an increased variability. Methods based on 6-DoF analysis generally yield fewer estimates for the summer months, likely related to lower CC values, as a threshold of 0.8 was applied. A dominant backazimuth direction can be identified during the winter season for all four methods, based on histograms weighted using the standard deviation ($\sigma$) according to

$$\text{weight} = 1 - \frac{\sigma}{\max\{\sigma\}}, \tag{3}$$

and with a bin width of 10°. Using a Gaussian KDE and median absolute deviation (MAD) definition, the maximum and the deviation are determined. A dominant direction of 254° ± 20° is derived for Love waves and for the Rayleigh waves 277° ± 23° or 268° ± 26° depending on the method (Rayleigh versus Tangent method; see Figs 2a–c).

Downloaded from academic.oup.com/gji/article/246/3/ggag285/8736044 by guest on 03 October 2026

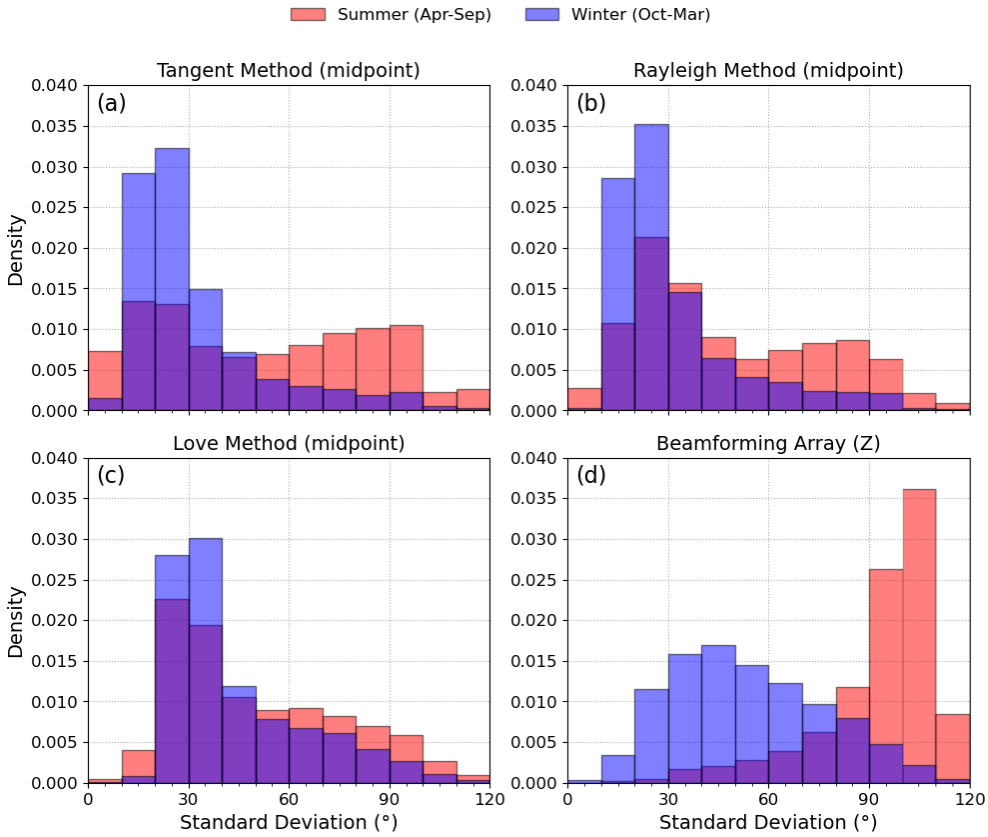


**Figure 3.** Histograms of standard deviations for backazimuth estimates are separately shown for the summer (April to September in red) and winter (October to March in blue) months of the Northern Hemisphere. Separate standard deviations based on (a) the Tangent method, (b) the Rayleigh method, (c) the Love method, and (d) array beamforming are presented.

The array-derived estimates, obtained via f–k beamforming of the vertical components, serve as the reference for Rayleigh waves. Here, a clear dominant direction of 295° ± 18° can be inferred for the winter months (Fig. 2d). For the summer months, the standard deviation of the backazimuth estimates increases significantly and a secondary direction of approximately 135° emerges (see Fig. 2d). While array beamforming can resolve two dominant directions better, the 6-DoF methods cannot.

Standard deviations of hourly backazimuth estimates vary seasonally, with a broader spread in the summer and a decrease in the winter. Most standard deviations for the 6-DoF-based methods range between 10° and 30° in winter (Figs 3a–c). Season-based standard deviations of hourly backazimuth estimates show a broader spread for the summer months, while a decrease occurs during the winter. For the 6-DoF-based methods, most standard deviations in the winter months range between 10° and 30°. The standard deviation count of the array-based backazimuth estimates spikes between 30° and 50° in the winter months and between 90° and 110° in the summer months (Fig. 3d).

Fig. 4 presents polar histograms of backazimuths on a stereographic map centered at the 6-DoF station. Notable distinctions in primary source directions emerge between summer and winter for the Tangent, Rayleigh, and Array methods, but not for the Love method. During summer, the Love method's southwestern direction at 254° becomes less prominent, though it maintains its direction. The Tangent method demonstrates a notable shift towards the southwest in summer, whereas a west–northwestern orientation prevails in winter. The Rayleigh method shows a similar, though more subtle, shift. Array data indicate a distinct secondary direction towards the southeast solely in summer, yet the west–northwest direction remains the more pronounced direction.

### 4.2 Backazimuth estimates of source maps

The generation mechanism of the secondary microseism is governed by nonlinear ocean wave–wave interactions. Consequently, the spatial distribution of the daily maximum SWH, measured with satellite altimetry, constitutes a valuable observational constraint for identifying potential source regions. Daily backazimuths inferred from inverted seismic ambient noise source maps provide an additional constraint to validate the 6-DoF station backazimuth estimates, which are aggregated into daily estimates using a weighted median, where the weights are determined by the backazimuth uncertainties.

Representative results for daily backazimuths obtained from the SWH data and from the 6-DoF analysis are presented in Fig. 5. On 25 January 2024 (Fig. 5a), enhanced wave activity is observed in the North Atlantic Ocean. Both SWH-based approaches yield broadly

Downloaded from academic.oup.com/gji/article/246/3/ggag285/8736044 by guest on 03 October 2026

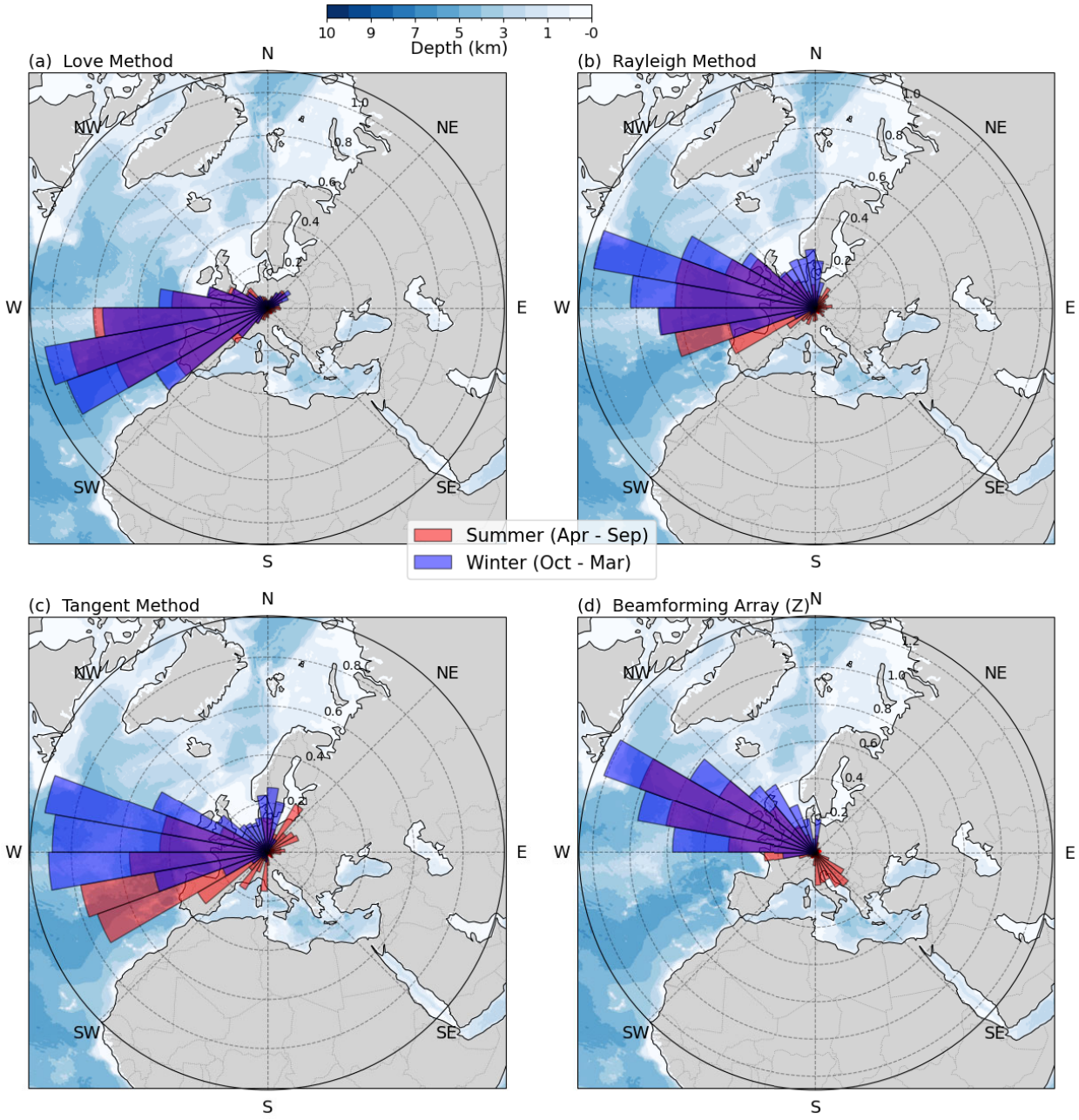


**Figure 4.** Histograms of hourly backazimuth estimates weighted by their deviation (see eq. 3) are separately shown for the summer (April to September) and winter (October to March) months on the Northern Hemisphere. The backazimuth estimates are based on (a) the Love method, (b) the Rayleigh method, (c) the Tangent method, and (d) array beamforming using the vertical component only.

consistent backazimuths, despite the presence of multiple regions with elevated wave heights on a global scale. The 6-DoF estimates exhibit overall agreement with these observations, with a maximal deviation of 16° for the Love waves. On 2024 February 11 (Fig. 5b), the dominant wave activity is located in the South Pacific, consistent with the source directions inferred from the 6-DoF methods.

For a representative summer day, 2024 May 2, the wave activity is distributed across several regions in the Southern Ocean, and the seismic-based backazimuth estimates display pronounced discrepancies (Fig. 5c).

Daily estimates of the dominant backazimuth direction inferred from SWH observations and SANS models are compared with the 6-DoF station estimates to assess the observed short-term and long-term variability in source direction. Results obtained using the distance-weighted integration scheme for the SWH and SANS data over the entire observation interval are displayed in Figs 6(a) and (b), respectively. A weak distance-weighting proportional to $R^{-1}$ is applied, thereby allowing for contributions from non-regional source areas. The SANS-based backazimuths exhibit a preference for source regions between approximately 270° and 20°, with a seasonal shift towards 160° and 240° during summer. For the SWH-based estimates, four distinct dominant directions are identified: two prevailing in summer at 130° and 210°, and two in winter at 280° and 360°. During winter, the dominant direction obtained from the seismic-based

Downloaded from academic.oup.com/gji/article/246/3/ggag285/8736044 by guest on 03 October 2026

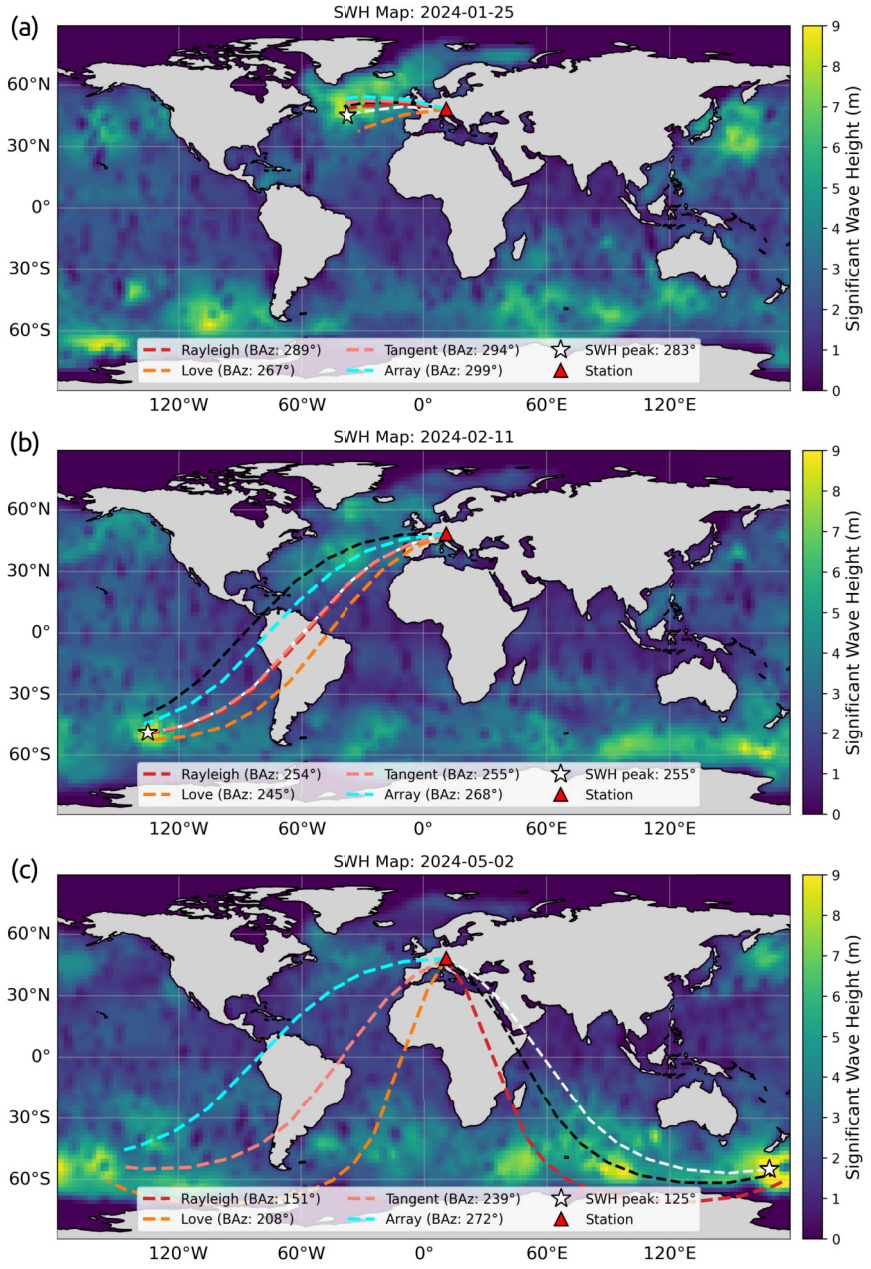


**Figure 5.** Backazimuth estimates are based on the low-pass filtered, daily maximal SWH map. Three example dates in 2024 are shown: (a) January 25, (b) February 11, and (c) May 02. A daily weighted median backazimuth is presented for all four methods (Rayleigh, Love, Tangent and Array). The 6-DoF station (red triangle), the obtained peak location of the SWH data (white star), and the integrated backazimuth estimate (black line) are indicated.

methods is consistent with the 280° direction (Northern Atlantic), whereas the 360° direction (Northern Pacific) is rarely resolved by either the 6-DoF station or the seismic array.

Daily differences between SWH-based and SANS-based results and the seismic-based results are computed for summer and winter separately and shown as distributions in Figs 6(c)–(j). Increased deviations are observed during summer, while in winter the distributions of deviations from the SWH-based backazimuths are quasi-unimodal and exhibit a systematic bias. The array beamforming approach yields the smallest mean deviation ($-20° \pm 34°$). The Rayleigh and Tangent methods provide comparable distributions and biases ($-36°$ and $-35°$), as anticipated, whereas the Love method exhibits a substantially larger mean deviation ($-50° \pm 54°$).

Downloaded from academic.oup.com/gji/article/246/3/ggag285/8736044 by guest on 03 October 2026

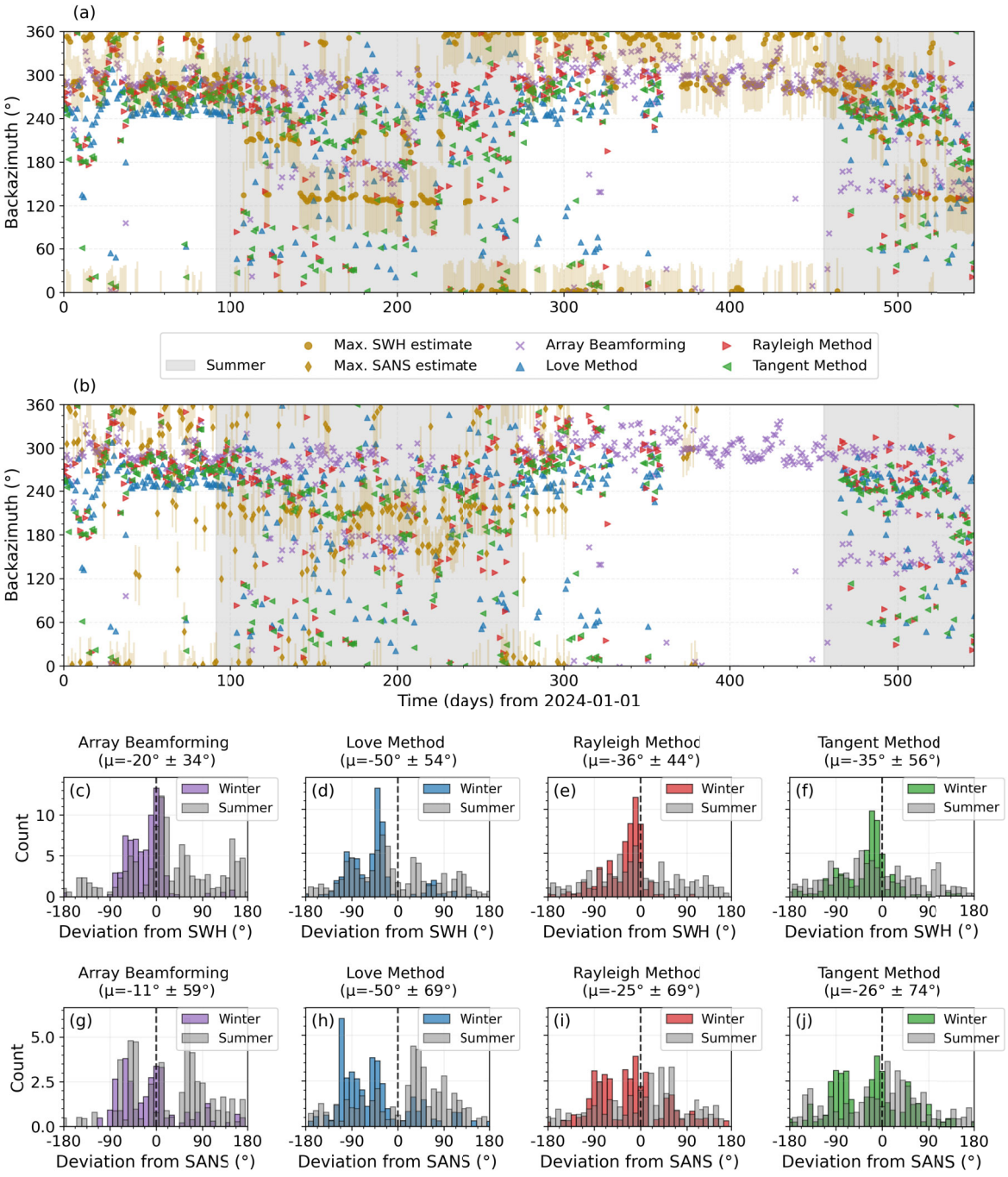


**Figure 6.** Comparison of the daily backazimuths inferred from (a) the observed significant wave height (SWH) activity (golden circles) and (b) the modelled maximal SANS activity (golden diamonds), with weighted median estimates of seismic-based methods over the entire observation period (2024-January-01 to 2025-June-30). The SWH-based and SANS-based estimates are scaled by distance: $R^{-1}$. Grey-shaded background areas indicate the summer months. The deviations of SWH-based as well as seismic-based estimates for the (c) array beamforming, (d) Love method, (e) Rayleigh method, (f) Tangent method and respectively for the deviations of the SANS-based maximal activity (g–j) are shown as weighted histograms, with bins of 10°, for the summer (shaded area) and winter (colour-coded). The mean ($\mu$) value and the standard deviation for the deviations in winter are annotated.

### 4.3 Pelagic storm tracking

The source mechanism of secondary microseismic noise is primarily attributed to nonlinear wave-wave interactions between ocean surface gravity waves during pelagic storm conditions (M.S. Longuet-Higgins 1950; R.K. Cessaro 1994; F. Ardhuin *et al.* 2011). Consequently, source regions can be associated with areas of elevated wave heights, which can be monitored using satellite altimetry. The use of seismic observations to track pelagic storms has previously been investigated (e.g. R.K. Cessaro & W.W. Chan 1989; J. Zhang

Downloaded from academic.oup.com/gji/article/246/3/ggag285/8736044 by guest on 03 October 2026

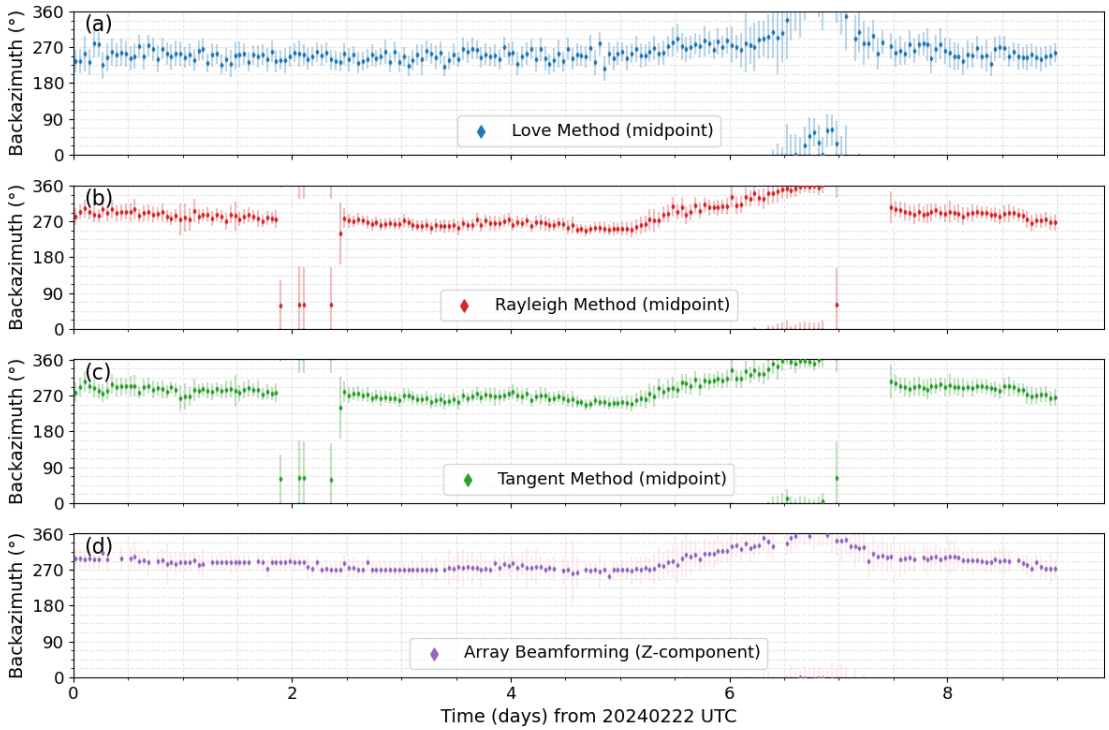


**Figure 7.** Hourly backazimuth estimates (markers) with assigned uncertainties (bars) are shown between 2024-February-22 to 2025-March-02 using (a) the Love method, (b) the Rayleigh method, (c) the Tangent method, and (d) array beamforming with the vertical component only.

*et al.* 2010; J.D. Peláez Quiñones *et al.* 2021), but only with translational data. However, the feasibility of storm tracking based on a 6-DoF methodology using single-station observations had not yet been demonstrated.

The time-series shown in Figs 2(b)–(c) exhibit pronounced, short-duration deviations (a few days) from the determined dominant backazimuth, predominantly heading northward. These backazimuth excursions on timescales of several days are a clearly observable feature, especially present during the winter months. Fig. 7 highlights one such excursion event occurring at the end of February 2024. The hourly estimates are generally stable and are characterized by small standard deviations. The apparently similar behaviour for the Rayleigh, Tangent, and Beamforming method results is expected because they are all based on Rayleigh-type wave energy.

Between the 2024 February 22nd and 27th, the backazimuth gradually drifts southward by about 45° to an absolute minimum of 250° before changing direction again and promptly drifting northward beyond 360° in just two days. This northward diversion from the dominant direction is also clearly evident in the backazimuth estimates of the Love method. On February 29 and March 01, however, the dominant backazimuth direction is re-established.

The daily maxima of satellite-based SWH measurements in the North Atlantic Ocean are used to qualitatively correlate the daily, weighted distributions of hourly backazimuth estimates in Fig. 8, using the Tangent method results (see Fig. 7c).

This demonstrates a successful tracking of a migrating pelagic storm across several days using the 6-DoF methods and observations of a single station. This is verified by seismic array beamforming and correlates well with significant wave height observations using satellite altimetry.

On February 26, the satellite data show two distinct centers of large wave heights, one in the Bay of Biscay (west of France) and a second south of Greenland and Iceland. Here, the backazimuth estimates point towards the closer area off France, likely exciting more seismic energy. The Rayleigh-based methods produced comparable results, while the Love wave method continues to point towards the Bay of Biscay, except for portions of February 28. The corresponding figures, showing results for these methods, are provided in the Supplementary Materials (Figs S2–S4).

## 5 DISCUSSION

We provide new insights on the monitoring of directivity of secondary microseismic noise with 6-DoF single-station methodologies for Love and Rayleigh waves. C. Hadziioannou *et al.* (2012) provided the first data-based backazimuth estimates for the secondary microseismic noise band, yet limited to *SH*-type (Love) waves due to the 4-DoF station. In our study, we provide results for Love and Rayleigh waves by using rotational ground motion measurements of horizontal components, which ROMY can provide at present with sufficient sensitivity for secondary microseismic noise. Data gaps in the observation interval over 1.5 years are mainly caused by

Downloaded from academic.oup.com/gji/article/246/3/ggag285/8736044 by guest on 03 October 2026

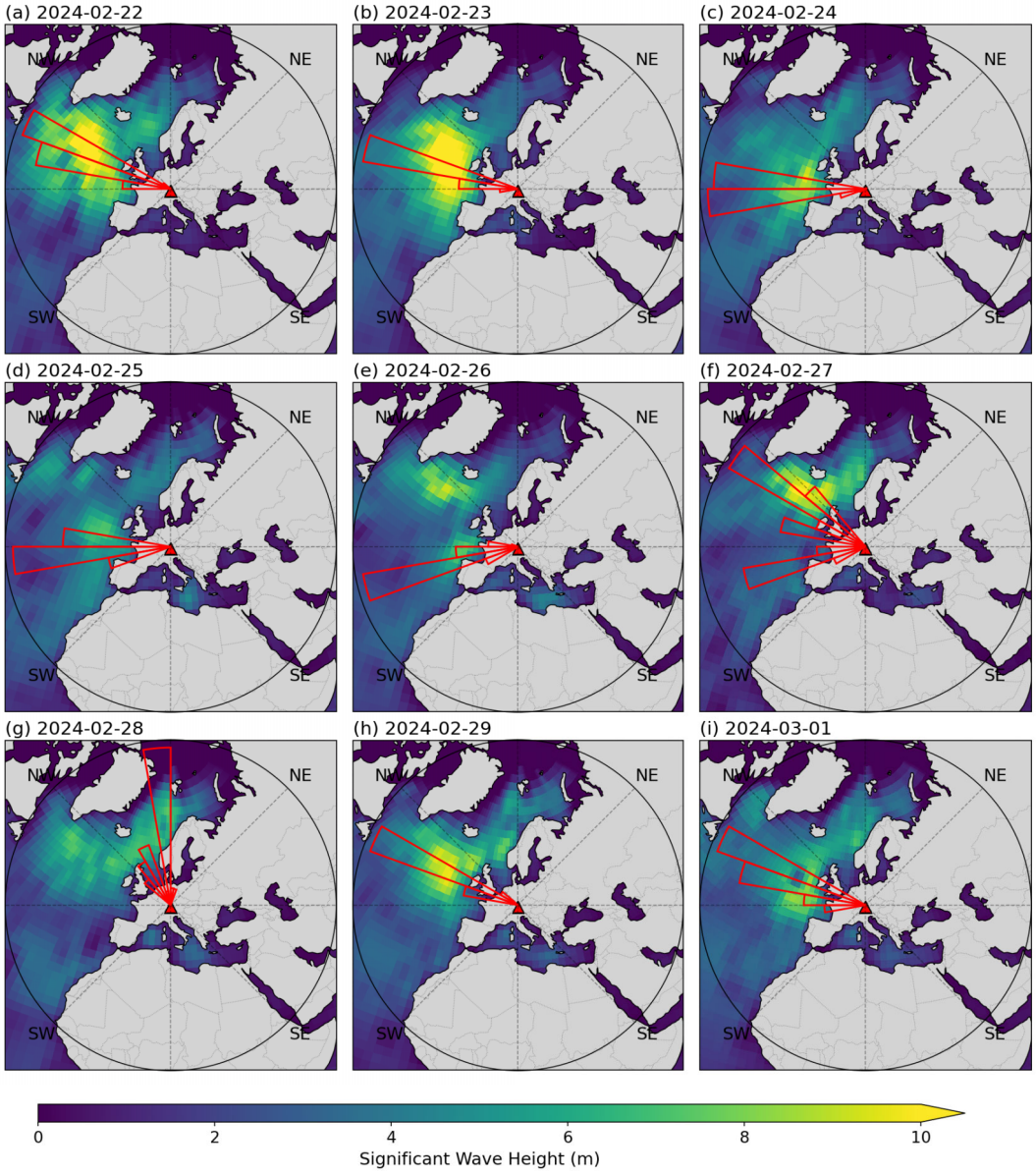


**Figure 8.** Panels (a) to (i) show maps of the daily maximum significant wave height inferred from satellite data (E.U. Copernicus Marine Service Information, CMEMS), clipped at 10 m, from 2024-February-22 to 2024-March-01. Overlaid are polar histograms of hourly backazimuth estimates of a single 6-DoF station for the same day, based on the Tangent method. The histograms are weighted by corresponding backazimuth uncertainties. The triangle marker denotes the location of the 6-DoF station.

outages or maintenance of at least one of ROMY's components. The current instrument performance and operational instabilities of ROMY are discussed by A. Brotzer *et al.* (2025a).

The potential of a single 6-DoF station to determine directions of secondary microseismic noise and temporal variations over 1.5 years is assessed. We systematically compare dominant backazimuth estimates of three 6-DoF methods: two sensitive to Rayleigh waves and one sensitive to Love waves, with established array beamforming for the vertical component, thus responsive to *SV*-type and Rayleigh waves. The horizontal components of the array stations exhibit elevated noise levels, attributable to their surface proximity, which compromises the reliability of array-derived rotations and, thus backazimuth estimates for Love waves. The array geometry constrains the frequency range for ADR and spatial differentiation across the array results in averaged gradients, implicitly assuming a common, rigid base across the array. In contrast, a single 6-DoF station provides broad-band, locally resolved gradients, although these may be more influenced by small-scale heterogeneities below the station.

A good agreement is found between the beamforming and 6-DoF methods (Rayleigh and Tangent) for the winter, whereas an absence of strong nearby sources in summer is reflected by a missing dominant direction and increased backazimuth uncertainties. Smaller standard deviations for hourly backazimuth estimates are indicated for the 6-DoF methods compared to the array beamforming.

Downloaded from academic.oup.com/gji/article/246/3/ggag285/8736044 by guest on 03 October 2026

For the parametrization, we derive hourly direction estimates maintaining a high temporal resolution while exploiting averaging and uncertainty quantification with high CC thresholds to emphasize plane waves, assuming stable sources over one hour. Knowing that source regions have a large extent (e.g. compared to activity on SWH maps or SANS maps) and not accounting for local or propagation effects, backazimuth bins of 10° provide meaningful results. Parameter adjustment could be evaluated if multiple distributed 6-DoF would be included in advanced localization schemes in future studies.

In the winter months, we find dominant source directions for the secondary microseism of 255° and 268° to 277° for Love and Rayleigh waves, respectively. With 295°, the dominant direction inferred from array beamforming deviates from the 6-DoF Rayleigh wave direction by about 20° towards North. A dominant source direction pointing to the Northern Atlantic Ocean is in agreement with other studies. C. Hadziioannou *et al.* (2012) investigated the backazimuth for two dates for both the G-ring laser (Love waves) and the nearby Gräfenberg array, with consistent noise sources at backazimuths of 270° and 280°, respectively. An analysis by A. Friedrich *et al.* (1998), also using the Gräfenberg array, identified several source regions for the secondary microseism in winter, of which SEC2 (290° to 310°) and SEC3 (255° to 265°) overlap with our dominant direction estimates. An analysis based on seismic arrays across Europe by C. Juretzek & C. Hadziioannou (2016) reveals that the source directions for Love and Rayleigh waves generally coincide with directions between about 280° and 320°. The systematic shift for the Love wave direction found in our study, pointing rather consistently towards the Bay of Biscay, could be related to a regional shelf, hence bathymetry-controlled Love wave generation (L. Gualtieri *et al.* 2021) alongside elevated wave activity in the Northern Atlantic.

In the summer months, the array beamforming resolves a second direction at around 135°, pointing towards increased activity in the Southern Ocean. The single station methods cannot resolve this secondary direction and a dominant direction only episodically for several days, mostly linked to nearby storms in the Atlantic Ocean. Hence, when there is only weak activity in nearby oceans and strong activity in the Southern Ocean, seismic waves of similar amplitude arrive from all directions, a dominant direction cannot be derived. A combination of source strength and distance appears to be decisive for dominance in the local wavefield and a dominant source is required for effective direction estimation with the single station.

In a more realistic Earth model, topography or heterogeneities along the propagation path can cause deviations from the great circle path, which can only be considered a first-order reference. Moreover, near-receiver, small-scale heterogeneities affect seismic gradients more than translations (e.g. S. Singh *et al.* 2019; S. Singh 2020), possibly explaining differences between translation-based ADR and direct rotation observations, which should be further investigated with a 3-D local subsurface model to explain parts of the observed bias. Another local site effect, strain-to-rotation coupling linked to local heterogeneities (e.g. J.C. Harrison 1976), might contribute to a local bias by affecting the translation and rotational signals differently. Modelling such effects to explain the observed systematic biases and the discrepancy between *SH*-type and *SV*-type waves, however, is beyond the scope of this observation-based study.

The generation of secondary microseisms is controlled by nonlinear wave–wave interactions. Therefore, satellite-based altimetry measurements of significant wave heights can be employed to identify regions of dominant ocean wave activity, hence potential source regions for secondary microseismic noise and their directions. H.S. Shabtian *et al.* (2023) report a clear correlation between the magnitude of the secondary microseismic noise and SWHs that reveal a seasonal variability. We use daily global maps of maximal SWHs from the Copernicus Marine Service to infer a dominant backazimuth and to compare our seismologically derived estimates with the observed spatially and temporally averaged ocean wave activity. As an alternative reference, we use the openly available seismic ambient source noise maps by J.K.H. Igel *et al.* (2023), which are model-based using a global seismic inversion approach (J.K.H. Igel *et al.* 2021b).

A simple selection of the maximum wave activity in the SWH or SANS maps would not incorporate any information on source-receiver distance. We therefore determine dominant backazimuth directions from distance-weighted distributions across backazimuths (see Supplementary Figs S7 and S9), and quantify corresponding uncertainties. These uncertainties generally range between 20° and 40°, and they also reflect the spatial resolution of the satellite data (2° × 2°). Distance weighting allows us to emphasize nearby sources, which reveals a dominant source direction with backazimuths between 270° and 10°, which is largely invariant over the annual cycle (see Fig. S9a in Supplementary Material). When allowing for more globally distributed sources, additional dominant directions appear with backazimuths between 110° and 240° during the summer months. This behaviour is consistent with the lack of a clear dominant direction of the 6-DoF-based estimates during summer, when much of the global ocean wave activity is located in the Southern Ocean and only infrequent, short-lived pelagic storms are present in the Northern Hemisphere. Under these conditions, spatially and temporally variable contributions from multiple, distinct source regions lead to a more complex locally observed seismic wavefield (see Figs 6a and b). Consequently, daily median backazimuths are less representative and the associated uncertainties increase during summer (see Figs 2 and 3). The deviations from the SWH-based and SANS-based references exhibit larger deviations in summer than in winter, with systematic biases present for all methods during winter, when a dominant direction exists. In winter, the smallest mean deviation is obtained for array beamforming (−20°), followed by the Rayleigh and Tangent methods (−36° and −35°, respectively), with the largest mean deviation for the Love method (−50°). This assessment is based on the assumption that plane waves propagate along great-circle paths from source to receiver, implying a simplified, isotropic, laterally homogeneous and 1-D Earth. Deviations from an expected great-circle-related backazimuth may therefore be caused by 3-D path effects as well as near-receiver site effects (e.g. strain-to-tilt coupling), which especially affect gradient-based methods (S. Singh 2020). Future 6-DoF seismic networks may improve SANS maps as local station effects can potentially be corrected for in translations, thus enhancing the translation-based inversion.

Downloaded from academic.oup.com/gji/article/246/3/ggag285/8736044 by guest on 03 October 2026

Multiple observed backazimuth changes over several days, diverting from the dominant source direction, can generally be attributed to transient teleseismic earthquakes on timescales of a few hours (e.g. A. Friedrich *et al.* 1998; C. Hadziioannou *et al.* 2012), or to migrating pelagic storms on timescales of a few days, as demonstrated in Section 4.3 (see Fig. 7). Here, the backazimuth estimates obtained from the Rayleigh/Tangent method and from array beamforming exhibit excellent agreement and jointly indicate a southward followed by a northward migration of the dominant source region (Figs 7b–d). For Love waves, the northward propagation is likewise clearly resolved (Fig. 7a). These observations can be directly associated with enhanced ocean wave activity in the northern Atlantic, where significant wave heights partially exceed 10 m (Fig. 8).

S. Yuan *et al.* (2021) demonstrate the potential of 6-DoF source tracking across multiple scales and for moving sources, simulating several 6-DoF sensors distributed around the source to increase the tracking accuracy. Future seismic networks of several 6-DoF stations with high-performance portable rotation sensors, for example, deployed around the North Atlantic Ocean, would enable the localization of secondary microseism sources in a manner analogous to that achieved with distributed seismic arrays.

## 6 CONCLUSIONS

We determine source directions of the secondary microseisms with a single 6-DoF station using *direct* observations of ground rotational motions for both Love and Rayleigh waves separately for the first time. High-quality rotational observations are provided by the ROMY ring laser gyroscope array, which provides all three components of weak motion and is sensitive enough to detect the secondary microseism peak.

We use 6-DoF processing to estimate backazimuths of Rayleigh and Love waves, which are comparable to results based on seismic array beamforming, especially for strong nearby sources during winter, with generally lower uncertainties for hourly estimates of the 6-DoF-based methods. We demonstrate the potential to successfully track a nearby pelagic storm over several days using 6-DoF methods with comparable results to array beamforming.

Reference source directions, derived from SHW and SANS data, exhibit a seasonal variability in dominant source directions, which generally agrees with directions estimated using array beamforming and the 6-DoF-based methods. During winter, we identify a dominant source direction of approximately 255° for Love (or *SH*-type) waves and between 268° and 277° for Rayleigh waves with 6-DoF-based single-station methods, whereas array beamforming yields 295°. Comparable directions are reported by other studies and support this proof-of-concept.

The southward deflection of approximately 20° (towards the Bay of Biscay) for the dominant direction of Love waves appears to be a robust observation, possibly linked to the source mechanism of Love waves or local site effects at the station and has to be addressed in future work. A discrepancy between SWH and SANS backazimuzh directions proxies and seismological results is anticipated due to 3-D path propagation effects, as well as site effects close to the receiver.

As a proof-of-concept, this study demonstrates the capability of a single 6-DoF station to determine source directions of secondary microseismic noise for Love and Rayleigh waves separately, similar to a seismic array. With the advent of portable high-performance rotation sensors, seismic networks can be upgraded to 6-DoF networks to enable seismic noise source localization of omnipresent ambient noise as well as storm tracking without seismic arrays.

## ACKNOWLEDGMENTS

The authors acknowledge the continuous support of the Faculty of Geosciences of the Ludwig-Maximilians-Universität München (Germany). This work relied on computational resources that were financed via the ‘Major Research Instrumentation’ programme funded by the Deutsche Forschungsgemeinschaft (DFG, German Research Foundation)-518204048. We gratefully acknowledge support from the European Research Council (ERC) for funding the ERC-Advanced ROMY Project (Grant number: 339991). We are grateful to the technical team, namely S. Egdorf, J. Loos and M. Terpoorten, for providing support for the ROMY project at the Geophysical Observatory in Fürstenfeldbruck, Germany. The authors express their gratitude for the constructive reviews, which have helped to further enhance the quality of this manuscript.

## SUPPORTING INFORMATION

Supplementary data are available at *GJIRAS* online.

**Figure S1.** In the upper panel, the waveforms for transverse translational acceleration of FUR (black) and vertical rotation rate of ROMY (red) are shown for one hour on 2024-February-21. The component combination filters for Love waves. The data are bandpass filtered between 0.1 and 0.15 Hz. The lower panel shows the backazimuth estimates in 48 s time windows (with 75 per cent overlap), colour-coded by the CC coefficient. Only estimates above a CC threshold of 0.8 are displayed. At the right end of the panel, the corresponding histogram and probability density function are shown. The theoretical backazimuth (dashed black line) is arbitrarily set to 300°.

Downloaded from academic.oup.com/gji/article/246/3/ggag285/8736044 by guest on 03 October 2026

**Figure S2.** Panels (a) to (i) show maps of the daily maximum significant wave height inferred from satellite data (E.U. Copernicus Marine Service Information, CMEMS) and the histogram of hourly backazimuth estimates of a single 6-DoF station, based on the Love method, for one day between 2024-February-22 and 2024-March-01. The triangle marker denotes the location of the 6-DoF station.

**Figure S3.** Panels (a) to (i) show maps of the daily maximum significant wave height inferred from satellite data (E.U. Copernicus Marine Service Information, CMEMS) and the histogram of hourly backazimuth estimates of a single 6-DoF station, based on the array beamforming (with the *Z*-component) for one day between 2024-February-22 and 2024-March-01. The triangle marker denotes the location of the 6-DoF station.

**Figure S4.** Panels (a) to (i) show maps of the daily maximum significant wave height inferred from satellite data (E.U. Copernicus Marine Service Information, CMEMS) and the histogram of hourly backazimuth estimates of a single 6-DoF station, based on the Rayleigh method, for one day between 2024-February-22 and 2024-March-01. The red marker denotes the location of the 6-DoF station.

**Figure S5.** Spectrograms of ROMY's (a) vertical, (b) north, and (c) east component between 2024-January-01 and 2024-May-31. The median power spectral density (PSD) with the 5th and 95th percentiles is shown in the side panels to the right.

**Figure S6.** Comparison of 6-DoF backazimuth estimation methods: Love method (upper panel), Rayleigh method (central panel), Tangent method (lower panel). Each estimate for a time window of 48 s with 75 per cent overlap is colour-coded by the CC value. Histograms of 10° bin width are shown on the right *y*-axis. The expected backazimuth is arbitrarily set to 300° (dashed line) with a ±10° error margin.

**Figure S7.** Three exemplary dates are presented: (a) 2024-January-25, (b) 2024-January-13, and (c) 2024-February-01, showing the low-pass filtered SWH map (left) and a distance-weighted polar histogram (right). The polar plot with respect to the 6-DoF station shows a histogram with 10° backazimuth bins, weighted by SWH values and the inverse distance ($R-1$). The associated Gaussian kernel density (KDE) function is shown with the determined peak and its deviation indicated. The 6-DoF station (triangle), the identified SWH peak (star) with great circle path, and the integration-based backazimuzh estimate are indicated in the map.

**Figure S8.** Three exemplary dates are presented: (a) 2024-January-13, (b) 2024-February-11, and (c) 2024-February-18, showing the SANS map (left) and a distance-weighted polar histogram (right). The polar plot with respect to the 6-DoF station shows a histogram with 10° backazimuth bins, weighted by SWH values and the inverse distance ($R-1$). The associated Gaussian kernel density (KDE) function is shown with the determined peak and its deviation indicated. The 6-DoF station (triangle), the identified SWH peak (star) with great circle path, and the integration-based backazimuzh estimate are indicated in the map.

**Figure S9.** Comparison of daily backazimuzh estimates using SWH and SANS data. A dominant backazimuth direction is estimated by identifying the global peak activity (blue circles) and based on the maximal kernel density of a distance-weighted histogram with 10° backazimuth bins (orange circles) with uncertainty. SWH-based results with distance scaling: (a) $R^{-2}$ and (b) $R^{-1}$, are shown. (c) SANS-based results are shown for available days using a distance scaling of $R^{-1}$.

**Figure S10.** Comparison of the daily backazimuths inferred from (a) the observed SWH activity (golden circles) and (b) the modelled maximal SANS activity (golden diamonds), with weighted median estimates of seismic-based methods over the entire observation period (2024-January-01 to 2025-June-30). The SWH-based and SANS-based estimates are scaled by distance: $R^{-2}$. Grey-shaded background areas indicate the summer months. The deviations of SWH-based as well as seismic-based estimates for the (c) array beamforming, (d) Love method, (e) Rayleigh method, (f) Tangent method, and respectively for the deviations of the SANS-based maximal activity (g–j) are shown as weighted histograms (bin width = 10°) for the summer (shaded area) and winter (colour-coded). The mean ($\mu$) value and the standard deviation for the deviations in winter are annotated.

Please note: Oxford University Press is not responsible for the content or functionality of any supporting materials supplied by the authors. Any queries (other than missing material) should be directed to the corresponding author for the paper.

## CONFLICT OF INTEREST

The authors acknowledge there are no conflicts of interest recorded.

## DATA AVAILABILITY

Observational data of the ROMY ring laser gyroscopes and the corresponding seismic array were provided by the Geophysical Observatory in Fürstenfeldbruck (BayernNetz 2001). Extensive parts of waveform data processing were done using modules of the ObsPy Python package (M. Beyreuther *et al.* 2010; T. Megies *et al.* 2011). This study has been conducted using E.U. Copernicus Marine Service Information: Global Ocean L4 Significant Wave Height from Nrt Satellite Measurements. E.U. Copernicus Marine Service Information (CMEMS). Marine Data Store (MDS). DOI: https://doi.org/10.48670/moi-00180 (Accessed on 2025-August-01)

Publicly available daily ambient seismic noise source maps, introduced by J.K.H. Igel *et al.* (2023), are used in this study. AI-assisted tools were used for language and grammar enhancement. All other data used in this study came from published sources listed in the references.

The project files, including processed data, notebooks, codes, and metadata, required to reproduce the figures and results presented in this study are provided in an online repository: https://syncandshare.lrz.de/getlink/fiNM5AYp8RvK5NsFyy9oop/GJI_SourceTracking and via Zenodo: https://doi.org/10.5281/zenodo.20403685. For more details, please contact the corresponding author.

Downloaded from academic.oup.com/gji/article/246/3/ggag285/8736044 by guest on 03 October 2026

## REFERENCES


Ardhuin, F., Stutzmann, E., Schimmel, M. & Mangeney, A., 2011. Ocean wave sources of seismic noise, *J. Geophys. Res.: Oceans,* **116**(C9).

Ardhuin, F., Gualtieri, L. & Stutzmann, E., 2015. How ocean waves rock the earth: two mechanisms explain microseisms with periods 3 to 300 s, *Geophys. Res. Lett.,* **42**(3), 765–772.

Bachmann, G.H. & Müller, M., 1992. Sedimentary and structural evolution of the german molasse basin, *Eclogae Geol. Helv.,* **85**(3), 519–530.

BayernNetz, 2001. *BayernNetz, Department of Earth and Environmental Sciences, Geophysical Observatory, University of Munich*. BayernNetz [Data set], International Federation of Digital Seismograph Networks. https://doi.org/10.7914/SN/BW

Bernauer, F., Wassermann, J. & Igel, H., 2012a. Rotational sensors—a comparison of different sensor types, *J. Seismol.,* **16**(4), 595–602.

Bernauer, M., Fichtner, A. & Igel, H., 2012b. Measurements of translation, rotation and strain: new approaches to seismic processing and inversion, *J. Seismol.,* **16**(4), 669–681.

Beyreuther, M., Barsch, R., Krischer, L., Megies, T., Behr, Y. & Wassermann, J., 2010. Obspy: a python toolbox for seismology, *Seismol. Res. Lett.,* **81**(3), 530–533.

Bormann, P., 2012. New Manual of Seismological Observatory Practice (NMSOP-2), *New Manual of Seismological Observatory Practice 2 (NMSOP2),* IASPEI, GFZ German Research Centre for Geosciences. Medium: application/pdf.

Brotzer, A. *et al.*, 2024. Characterizing the background noise level of rotational ground motions on Earth, *Seismol. Res. Lett.,* **95**(3), 1858–1869.

Brotzer, A., Igel, H., Bernauer, F., Wassermann, J., Kodet, J., Schreiber, K.U., Zenner, J. & Stellmer, S., 2025a. On environment-related instrumental effects of ROMY (ROtational Motions in seismologY): a prototype, multi-component, heterolithic ring laser array, *Rev. Sci. Instrum.,* **96**(6), 064502.

Brotzer, A., Igel, H., Bernauer, F., Wassermann, J., Mellors, R. & Vernon, F., 2025b. On single-station, six degree-of-freedom observations of local to regional seismicity at the Piñon Flat Observatory in Southern California, *Seismica,* **4**(1).

Cessaro, R.K., 1994. Sources of primary and secondary microseisms, *Bull. seism. Soc. Am.,* **84**(1), 142–148.

Cessaro, R.K. & Chan, W.W., 1989. Wide-angle triangulation array study of simultaneous primary microseism sources, *J. Geophys. Res.: Solid Earth,* **94**(B11), 15555–15563.

Chevrot, S., Sylvander, M., Benahmed, S., Ponsolles, C., Lefèvre, J.M. & Paradis, D., 2007. Source locations of secondary microseisms in western Europe: evidence for both coastal and pelagic sources, *J. Geophys. Res.: Solid Earth,* **112**(B11).

Cochard, A. *et al.*, 2006. Rotational motions in seismology: theory, observation, simulation, in *Earthquake Source Asymmetry, Structural Media and Rotation Effects,* pp. 391–411, Springer.

Essen, H.H., Krüger, F., Dahm, T. & Grevemeyer, I., 2003. On the generation of secondary microseisms observed in northern and central Europe, *J. Geophys. Res.: Solid Earth,* **108**(B10)..

Flinn, E., 1965. Signal analysis using rectilinearity and direction of particle motion, *Proc. IEEE,* **53**(12), 1874–1876.

Friedrich, A., Krüger, F. & Klinge, K., 1998. Ocean-generated microseismic noise located with the Gräfenberg array, *J. Seismol.,* **2**(1), 47–64.

Gualtieri, L., Stutzmann, E., Capdeville, Y., Farra, V., Mangeney, A. & Morelli, A., 2015. On the shaping factors of the secondary microseismic wavefield, *J. Geophys. Res.: Solid Earth,* **120**(9), 6241–6262.

Gualtieri, L., Stutzmann, E., Juretzek, C., Hadziioannou, C. & Ardhuin, F., 2019. Global scale analysis and modelling of primary microseisms, *Geophys. J. Int.,* **218**(1), 560–572.

Gualtieri, L., Bachmann, E., Simons, F.J. & Tromp, J., 2021. Generation of secondary microseism love waves: effects of bathymetry, 3-D structure and source seasonality, *Geophys. J. Int.,* **226**(1), 192–219.

Gutenberg, B., 1912. Die seismische bodenunruhe, gerlands beitr, *Geophysics,* **11,** 314–361

Gutenberg, B., 1921. *Untersuchungen über die Bodenunruhe mit Perioden von 4s-10s in Europa,* Bureau central de séismologie de l'union géodesique et géophysique.

Gutenberg, B., 1936. On microseisms, *Bull. seism. Soc. Am.,* **26**(2), 111–117.

Hadziioannou, C., Gaebler, P., Schreiber, U., Wassermann, J. & Igel, H., 2012. Examining ambient noise using colocated measurements of rotational and translational motion, *J. Seismol.,* **16**(4), 787–796.

Harrison, J.C., 1976. Cavity and topographic effects in tilt and strain measurement, *J. geophys. Res. (1896–1977),* **81**(2), 319–328.

Hasselmann, K., 1963. A statistical analysis of the generation of microseisms, *Rev. Geophys.,* **1**(2), 177–210.

Hillers, G., Graham, N., Campillo, M., Kedar, S., Landès, M. & Shapiro, N., 2012. Global oceanic microseism sources as seen by seismic arrays and predicted by wave action models, *Geochem. Geophys. Geosyst.,* **13**(1).

Igel, H., Schreiber, U., Flaws, A., Schuberth, B., Velikoseltsev, A. & Cochard, A., 2005. Rotational motions induced by the M8.1 Tokachi-oki earthquake, September 25, 2003, *Geophys. Res. Lett.,* **32**(8)..

Igel, H., Cochard, A., Wassermann, J., Flaws, A., Schreiber, U., Velikoseltsev, A. & Pham Dinh, N., 2007. Broad-band observations of earthquake-induced rotational ground motions, *Geophys. J. Int.,* **168**(1), 182–196.

Igel, H., Bernauer, M., Wassermann, J. & Schreiber, K.U., 2014. Seismology, Rotational, Complexity, in *Encyclopedia of Complexity and Systems Science,* pp. 1–26, eds. Meyers, R.A., Springer, Berlin.

Igel, H. *et al.*, 2021a. ROMY: a multicomponent ring laser for geodesy and geophysics, *Geophys. J. Int.,* **225**(1), 684–698.

Igel, J.K.H., Ermert, L.A. & Fichtner, A., 2021b. Rapid finite-frequency microseismic noise source inversion at regional to global scales, *Geophys. J. Int.,* **227**(1), 169–183.

Igel, J.K.H., Bowden, D.C. & Fichtner, A., 2023. SANS: publicly available daily multi-scale seismic ambient noise source maps, *J. Geophys. Res.: Solid Earth,* **128**(1), e2022JB025114.

Izgi, G., Eibl, E.P., Krueger, F. & Bernauer, F., 2025. Direction finding in an active source experiment in fürstenfeldbruck, germany using 6 dof measurements, *Geophys. J. Int.,* **240**(3), 2042–2059.

Juretzek, C. & Hadziioannou, C., 2016. Where do ocean microseisms come from? A study of Love-to-Rayleigh wave ratios, *J. Geophys. Res.: Solid Earth,* **121**(9), 6741–6756.

Juretzek, C. & Hadziioannou, C., 2017. Linking source region and ocean wave parameters with the observed primary microseismic noise, *Geophys. J. Int.,* **211**(3), 1640–1654.

Keil, S., Wassermann, J. & Igel, H., 2021. Single-station seismic microzonation using 6C measurements, *J. Seismol.,* **25**(1), 103–114.

Kislov, K. & Gravirov, V., 2021. Rotational seismology: Review of achievements and outlooks, *Seismic Instrum.,* **57**(2), 187–202.

Langston, C.A. & Liang, C., 2008. Gradiometry for polarized seismic waves, *J. Geophys. Res.: Solid Earth,* **113**(B8).


Downloaded from academic.oup.com/gji/article/246/3/ggag285/8736044 by guest on 03 October 2026

Le Pape, F., Craig, D. & Bean, C.J., 2021. How deep ocean-land coupling controls the generation of secondary microseism Love waves, *Nat. Commun.,* **12**(1), 2332.
Longuet-Higgins, M.S., 1950. A theory of the origin of microseisms, *Philos. Trans. R. Soc. London Ser. A: Math. Phys. Sci.,* **243**(857), 1–35.
Megies, T., Beyreuther, M., Barsch, R., Krischer, L. & Wassermann, J., 2011. Obspy–what can it do for data centers and observatories?, *Ann. Geophys.,* **54**(1), 47–58.
Pancha, A., Webb, T.H., Stedman, G.E., McLeod, D.P. & Schreiber, K.U., 2000. Ring laser detection of rotations from teleseismic waves, *Geophys. Res. Lett.,* **27**(21), 3553–3556.
Peláez Quiñones, J.D., Becker, D. & Hadziioannou, C., 2021. Beamforming of Rayleigh and Love waves in the course of Atlantic cyclones, *J. Geophys. Res.: Solid Earth,* **128,** e2022JB025050.
Safarkhani, M., Schippkus, S. & Hadziioannou, C., 2025. Imprints of time-dependent microseism source distributions on the coda of correlations, *Geophys. J. Int.,* **243**(2), ggaf358.
Schimmel, M., Stutzmann, E., Ardhuin, F. & Gallart, J., 2011. Polarized Earth's ambient microseismic noise, *Geochem. Geophys. Geosyst.,* **12**(7).
Schmelzbach, C. *et al.*, 2018. Advances in 6C seismology: Applications of combined translational and rotational motion measurements in global and exploration seismology, *Geophysics,* **83**(3), WC53–WC69.
Schreiber, K.U., Klügel, T., Velikoseltsev, A., Schlüter, W., Stedman, G.E. & Wells, J.P.R., 2009. The large ring laser G for continuous earth rotation monitoring, *Pure appl. Geophys.,* **166**(8–9), 1485–1498.
Shabtian, H.S., Eilon, Z.C. & Tanimoto, T., 2023. Seasonality of California Central coast microseisms, *Bull. seism. Soc. Am.,* **114**(2), 873–881.
Singh, S., 2020. Wavefield gradients and small-scale heterogeneities, *Earth Sciences, Doctoral Thesis*, Université de Nantes.
Singh, S., Capdeville, Y. & Igel, H., 2019. Correcting wavefield gradients for the effects of local small-scale heterogeneities, *Geophys. J. Int.,* **220**(2), 996–1011.
Sollberger, D. *et al.*, 2020. Seismological processing of six degree-of-freedom ground-motion data, *Sensors,* **20**(23), 6904.
Spudich, P. & Fletcher, J.B., 2008. Observation and prediction of dynamic ground strains, tilts, and torsions caused by the Mw 6.0 2004 Parkfield, California, Earthquake and Aftershocks, derived from UPSAR array observations, *Bull. seism. Soc. Am.,* **98**(4), 1898–1914.
Stutzmann, E., Ardhuin, F., Schimmel, M., Mangeney, A. & Patau, G., 2012. Modelling long-term seismic noise in various environments, *Geophys. J. Int.,* **191**(2), 707–722.
Tang, L., Igel, H., Montagner, J.P., Hadziioannou, C., Safarkhani, M. & Vernon, F.L., 2024. Seasonality of microseisms in Southern California from 6C ground motions, ESS Open Archive (preprint).
Tanimoto, T. & Anderson, A., 2023. Seismic noise between 0.003 Hz and 1.0 Hz and its classification, *Prog. Earth Planet. Sci.,* **10**(1), 56.
Tanimoto, T., Hadziioannou, C., Igel, H., Wasserman, J., Schreiber, U. & Gebauer, A., 2015. Estimate of Rayleigh-to-Love wave ratio in the secondary microseism by colocated ring laser and seismograph, *Geophys. Res. Lett.,* **42**(8), 2650–2655.
Tanimoto, T., Lin, C., Hadziioannou, C., Igel, H. & Vernon, F., 2016. Estimate of Rayleigh-to-Love wave ratio in the secondary microseism by a small array at Piñon Flat observatory, California, *Geophys. Res. Lett.,* **43**(21).
Wassermann, J., Braun, T., Ripepe, M., Bernauer, F., Guattari, F. & Igel, H., 2022. The use of 6DOF measurement in volcano seismology–a first application to Stromboli volcano, *J. Volc. Geotherm. Res.,* **424,** 107499.
Wiechert, E., 1904. Discussion, verhandlung der zweiten internationalen seismologischen konferenz, gerl, *Beitr. Geophys.,* **2,** 41–43.
Yuan, S., Simonelli, A., Lin, C.J., Bernauer, F., Donner, S., Braun, T., Wassermann, J. & Igel, H., 2020. Six degree-of-freedom broadband ground-motion observations with portable sensors: validation, local earthquakes, and signal processing, *Bull. seism. Soc. Am.,* **110**(3), 953–969.
Yuan, S., Gessele, K., Gabriel, A.A., May, D.A., Wassermann, J. & Igel, H., 2021. Seismic source tracking with six degree-of-freedom ground motion observations, *J. Geophys. Res.: Solid Earth,* **126**(3), e2020JB021112.
Yuan, S., Bernauer, F., Wassermann, J., Martin, E.R. & Igel, H., 2025. Single-station vehicle tracking using six-component seismic measurements: a comparative study with array-based methods, *Seismica,* **4**(2).
Zhang, J., Gerstoft, P. & Bromirski, P.D., 2010. Pelagic and coastal sources of P-wave microseisms: generation under tropical cyclones, *Geophys. Res. Lett.,* **37**(15).
Ziane, D. & Hadziioannou, C., 2019. The contribution of multiple scattering to Love wave generation in the secondary microseism, *Geophys. J. Int.,* **217**(2), 1108–1122.

Downloaded from academic.oup.com/gji/article/246/3/ggag285/8736044 by guest on 03 October 2026

© The Author(s) 2026. Published by Oxford University Press on behalf of The Royal Astronomical Society. This is an Open Access article distributed under the terms of the Creative Commons Attribution License (https://creativecommons.org/licenses/by/4.0/), which permits unrestricted reuse, distribution, and reproduction in any medium, provided the original work is properly cited.